Review of Scientific Instruments

Automated source of squeezed vacuum states driven by finite state machine based software

Cite as: Rev. Sci. Instrum. **92**, 054504 (2021); https://doi.org/10.1063/5.0046317
Submitted: 02 February 2021 • Accepted: 05 May 2021 • Published Online: 24 May 2021

C. Nguyen, M. Bawaj, V. Sequino, et al.

Review of Scientific Instruments ARTICLE scitation.org/journal/rsi

Automated source of squeezed vacuum states driven by finite state machine based software

Cite as: Rev. Sci. Instrum. 92, 054504 (2021); doi: 10.1063/5.0046317
Submitted: 2 February 2021 • Accepted: 5 May 2021 •
Published Online: 24 May 2021

C. Nguyen,[1] M. Bawaj,[2,3,a)] V. Sequino,[4,5,a)] M. Barsuglia,[1] M. Bazzan,[6,7] E. Calloni,[4,5] G. Ciani,[6,7] L. Conti,[7] B. D'Angelo,[8,9] R. De Rosa,[4,5] L. Di Fiore,[5] S. Di Pace,[10,11] V. Fafone,[12,13] B. Garaventa,[8,9] A. Gennai,[14] L. Giacoppo,[10,11,12] I. Khan,[13,15,16] M. Leonardi,[17,18,19] E. Majorana,[10,11] L. Naticchioni,[10,11] F. Paoletti,[14] D. Passuello,[14] M. Pegoraro,[7] F. Ricci,[10,11] A. Rocchi,[13] M. Vardaro,[6,20,21] H. Vocca,[2,3] J.-P. Zendri,[7] M. De Laurentis,[4,5] and F. Sorrentino[8]

AFFILIATIONS

[1]Université de Paris, CNRS, Astroparticule et Cosmologie, F-75006 Paris, France
[2]INFN, Sezione di Perugia, I-06123 Perugia, Italy
[3]Università di Perugia, I-06123 Perugia, Italy
[4]Università di Napoli "Federico II", I-80126 Napoli, Italy
[5]INFN, Sezione di Napoli, I-80126 Napoli, Italy
[6]Università di Padova, I-35131 Padova, Italy
[7]INFN, Sezione di Padova, I-35131 Padova, Italy
[8]INFN, Sezione di Genova, I-16146 Genova, Italy
[9]Università degli Studi di Genova, I-16146 Genova, Italy
[10]Università di Roma "La Sapienza", I-00185 Roma, Italy
[11]INFN, Sezione di Roma, I-00185 Roma, Italy
[12]Università di Roma "Tor Vergata", I-00133 Roma, Italy
[13]INFN, Sezione di Roma "Tor Vergata", I-00133 Roma, Italy
[14]INFN, Sezione di Pisa, I-56127 Pisa, Italy
[15]Gran Sasso Science Institute (GSSI), I-67100 L'Aquila, Italy
[16]Aix Marseille University, CNRS, Centrale Marseille, Institut Fresnel, Marseille, France
[17]INFN, Trento Institute for Fundamental Physics and Applications, I-38123 Povo, Italy
[18]Università di Trento, I-38123 Povo, Italy
[19]National Astronomical Observatory of Japan, 2-21-1 Osawa, Mitaka, Tokyo, 181-8588, Japan
[20]Institute for High-Energy Physics, University of Amsterdam, Science Park 904, 1098 XH Amsterdam, Netherlands
[21]Nikhef, Science Park 105, 1098 XG Amsterdam, Netherlands

[a)]**Authors to whom correspondence should be addressed:** mateusz.bawaj@pg.infn.it and valeria.sequino@na.infn.it

ABSTRACT

In the last few decades, much effort has been made for the production of squeezed vacuum states in order to reduce quantum noise in the audio-frequency band. This technique has been implemented in all running gravitational-wave interferometric detectors and helped to improve their sensitivity. While the detectors are acquiring data for astrophysical observations, they must be kept in the operating condition, also called "science mode," that is, a state that requires the highest possible duty-cycle for all the instrumental parts and controls. We report the development of a highly automated setup for the generation of optical squeezed states, where all the required control loops are supervised by a software based on finite state machines; we took special care to grant ease of use, stability of operation, and possibility of auto-recovery. Moreover, the setup has been designed to be compatible with the existing software and hardware infrastructure of

the Virgo detector. In this paper, we discuss the optical properties of this squeezing setup, the locking techniques, and the automation algorithms.

 https://doi.org/10.1063/5.0046317

I. INTRODUCTION—STATE OF THE ART

On September 14, 2015, the first direct detection of Gravitational Wave (GW) from the merger of two coalescing black holes[1] opened a new window to observe the Universe. The first detection was followed by many more,[2,3] collected by the global network of Advanced Laser Interferometer Gravitational-Wave Observatory (LIGO) and Advanced Virgo in a series of coordinated observation periods; these have been interleaved by periods of major upgrades of the detectors, which resulted in an increased rate of detections. These improvements are mainly targeted to the reduction of the noises.

Quantum Noise (QN) is a fundamental source of noise in an interferometric detector and is due to the vacuum fluctuations entering from the interferometer output port. In particular, quantum phase and amplitude fluctuations are responsible for the so-called Shot Noise (SN) and Radiation Pressure Noise (RPN), respectively.[4] Before the upgrades, foreseen for the fourth observation run (O4), only the SN has limited the sensitivity of GW detectors in a frequency band from 100 Hz up to 10 kHz, while the RPN, which dominates the QN at lower frequencies, was covered by technical noises.

In 1981, Caves proposed a technique based on the production of squeezed vacuum states, which allows us to decrease the SN at the expense of increasing the RPN.[4] Caves' idea was to replace the ordinary electromagnetic vacuum, entering the dark port of the interferometer, with a squeezed vacuum field. Squeezed states are characterized by unequal phase and amplitude quadrature variances. They were observed for the first time in 1985[5] in the radio-frequency band. Broadband optical squeezed states in the GW detection band, i.e., from 10 Hz up to 10 kHz, were demonstrated for the first time in 2006[6] using an Optical Parametric Oscillator (OPO). In the last decade, vacuum squeezed states, produced by degenerate optical parametric oscillation, have been injected in GW interferometers (GEO600, Advanced LIGO and Advanced Virgo), and the efficiency of this technique in improving the GW detector sensitivity was experimentally demonstrated.[7–9] During the data-taking period, when the detector is in *science mode*, a high duty-cycle of the squeezing source is required. In Ref. 8, the squeezing injection duty-cycle is reported to be above 99%. For this reason, we have developed a squeezing facility with the aim to test new techniques and improve control strategies using a software based on Finite-State Machine (FSM). FSM is a mathematical concept used in automata theory to describe an automation mechanism that can change from one state to another in response to input signals. An FSM is defined by a list of states and the inputs that trigger transitions. The idea of automation of the squeezing experiment using digital hardware has already been proposed.[10] In this article, we expand that basic idea, and we present a working proof-of-principle. Finally, the analysis of the developed system is reported in this paper. Particular attention is paid to the ratio of the working time requested from each control loop and the real time of the working condition, namely, Quality of Service (QoS). The recovery time is not intended as the working condition and thus reduces the QoS of our system.

II. OPTICAL SETUP

The optical layout of the experiment, shown in Fig. 1, is based on the design of the squeezer developed by the Albert Einstein Institute,[11] which is currently used in GEO600 and Advanced Virgo.[8] A Nd:YAG main laser provides an 1 W S-polarized beam at 1064 nm, which is split into three as follows: a pump beam for the Second-Harmonic Generation (SHG), a Bright Alignment Beam (BAB), and a Local Oscillator (LO) used for the homodyne detection. The second-harmonic beam, produced by the SHG, is stabilized in power by a Mach–Zehnder (MZ) interferometer, and its spatial mode is filtered by a mode-cleaner cavity, Mode Cleaner Green (MCG). The resulting beam acts as a pump for the Optical Parametric Oscillator (OPO). The BAB is used for OPO cavity alignment, matching with the pump beam, and homodyne detector alignment and as a bright beam to check the co-resonance between the

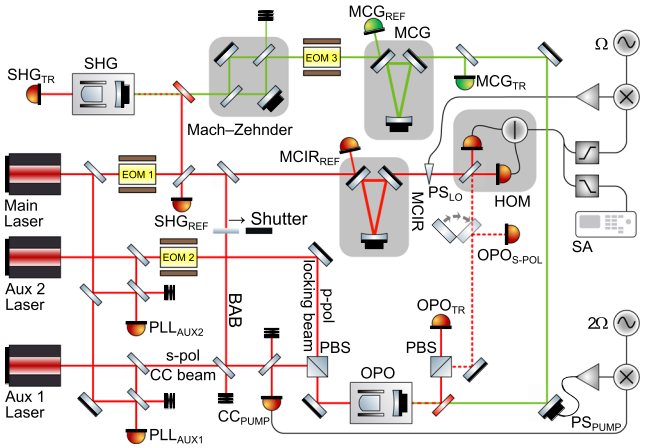

FIG. 1. Optical layout of our squeezing experiment. The main laser, with an output power of 1 W, provides the main carrier frequency for the Local Oscillator (LO) and frequency doubling in the Second-Harmonic Generation (SHG) cavity. Aux 1 and Aux 2 lasers, with an output power of 170 mW, are phase-locked to the main laser by Optical Phase-Locked Loop (OPLL) that uses the beat note obtained by the two photo-detectors PLL_{Aux1} and PLL_{Aux2}. These lasers provide the Optical Parametric Oscillator (OPO) locking beam and the Coherent Control (CC) beam. Triangular cavities Mode Cleaner Green (MCG) and Mode Cleaner Infrared (MCIR) are used for spatial mode-cleaning of the pump and the LO beams. The Mach–Zehnder (MZ) interferometer stabilizes the power of the second harmonic field used as the OPO pump. In the scheme, all photo-detectors used for the locking are indicated. Only CC lock scheme components are depicted. Schematics of the remaining loops are explained further in this article. Phase shifters PS_{LO} and PS_{PUMP} are the actuators driven by local oscillator coherent control (CC_{LO}) and pump beam coherent control (CC_{PUMP}) loops, respectively.

P-polarized locking beam and the S-polarized squeezed vacuum field. The LO is spatially filtered by a Mode Cleaner Infrared (MCIR) cavity, built in the same configuration as the one used for the green pump beam, before reaching the homodyne detector. An auxiliary laser (Aux 2), phase-locked to the main laser by an Optical Phase-Locked Loop (OPLL), provides the above-mentioned locking beam for the control of the OPO cavity length. Another auxiliary laser (Aux 1), also phase-locked to the main laser and S-polarized, is used to implement the phase control of the generated squeezed light field. Finally, the generated squeezed light level is measured using a balanced homodyne detector that is able to measure squeezing in both radio and audio-frequency bands.

A. Nonlinear cavities

The two nonlinear interactions, SHG and OPO, are realized using Periodically Poled Potassium Titanyl Phosphate (PPKTP) crystals, having a High Reflectivity (HR) curved face to form a hemilithic cavity with an in-coupling mirror, thus providing a stable and compact configuration with low intracavity losses. Crystal dimensions are $1 \times 1.5 \times 9.3$ mm,[3] and the Radius of Curvature (RoC) of the curved face is 8 mm. The coupling mirror has a RoC = 25 mm, and its reflectivity at 1064 nm is $R_{1064} = 90\%$ for the SHG and $R_{1064} = 92\%$ for the OPO. The distance between this mirror and the flat face of the crystal is 22 mm. In-cavity SHG is employed in our experiment to generate the squeezing pump beam at 532 nm. The coupling mirror is connected to a piezoelectric actuator so that the SHG also acts as the scanning cavity. SHG finesse at 1064 nm is $\mathcal{F} = 54$, with a Free Spectral Range (FSR) of about 3.8 GHz, corresponding to a Full Width at Half Maximum (FWHM) of about 71 MHz. The achieved SHG conversion efficiency is more than 60% at the optimal phase-matching temperature of 31.6 °C. This conversion efficiency is sufficient for our experiment, but, as it has been demonstrated in Ref. 12, under certain conditions, with the same cavity, it is possible to reach a conversion efficiency of about 99%.

B. Pump beam power stabilization

As demonstrated by the experience in GEO600,[13] fluctuations of the OPO pump power can lead to the degradation of the squeezing level, especially during long-term operation. Another effect of these fluctuations is the variation of the OPO crystal refractive index due to its temperature fluctuation, with a consequent loss of the phase-matching condition. A closed-loop temperature control is used to keep the crystal at a stable temperature within an rms fluctuation of 3 mK. Moreover, it affects the correct operation of the coherent control technique, described in Sec. II D. For this reason, the intensity of the pump beam is stabilized by an active control using a MZ interferometer whose two output beams are used, one for the interferometer length control and the other one to pump the OPO. On the optical path, MZ is placed in front of the MCG, which might lead to an undesired unlock of the latter. This does not happen because the limited visibility of the MZ is 18% while the MCG unlock threshold is set beneath the actuation range of the MZ. In order to control the length of this interferometer, and thus its transmission, the length of one of the two arms is controlled by means of a piezoelectric actuated mirror.

TABLE I. Spectral properties of the traveling-wave mode-cleaner cavities.

	FSR (MHz)	FWHM (MHz)	$\mathcal{F}$	λ (mm)
MCG	515	5	101	532
MCIR	550	7.7	71.3	1064

C. Mode cleaner triangular cavities

In order to suppress higher order modes, inside the OPO, the beam is spatially and frequency-cleaned by an external triangular cavity resonant on the fundamental TEM00 mode. The travelling-wave resonator configuration makes a polarization filtering of the pump beam as well. This cavity is composed of two plane mirrors and a curved one with a RoC of 1 m. In order to ensure thermo-mechanical stability, the optical elements are mechanically mounted on an INVAR spacer whose thermal expansion coefficient is $\alpha = 1.2 \times 10^{-6}$ K^{-1}. The cavity length is controlled by a piezoelectric actuator attached to the rear of the curved mirror. A similar cavity is used for the LO beam in order to improve the overlap with the squeezed beam coming from the OPO. The spectral properties of these two cavities are shown in Table I.

D. OPO length control and coherent control technique

In order to use the squeezing technique at the frequencies of interest for GW detectors, the phase of the pump beam and of the LO must be controlled in order to have a stable phase-locking of the squeezed states. For the production of squeezed vacuum states, the OPO cavity must be seeded by a pure vacuum field. This would make it impossible to control the cavity length by using the standard Pound–Drever–Hall technique (PDH technique), which requires the modulation of a bright beam with a carrier frequency resonant inside the cavity.[14] As proposed in Ref. 6 (see Fig. 1), we use an auxiliary beam with an orthogonal polarization with respect to that of the squeezed vacuum field. Due to the birefringence of the nonlinear crystal inside the OPO, the resonance conditions of S- and P-polarized beams are frequency offset with respect of each other; therefore, the field for the length control of the OPO cannot be provided by the main laser. For this reason, an external laser (Aux 2) is used, with its frequency being kept shifted with respect to the one of the main lasers, in order to have the co-resonance of the two beams inside the OPO. This frequency shift is kept constant using one of the OPLL, described in Sec. II E. Another auxiliary beam, called Coherent Control Beam (CCB), is used to control the quadrature angle of the squeezed field. This beam has the same polarization as the squeezed beam, and it does sense the non-linearity of the OPO. Its frequency shift $\Omega = 7$ MHz, with respect to the squeezed-vacuum frequency, falls within the OPO linewidth. Hence, it will be turned in a field with amplified and deamplified quadratures. The reflected beam, demodulated at 2Ω, provides the error signal that is used to fix the phase relation between the CCB and the second harmonic OPO pump field; the actuation point of this loop is a mirror along the pump beam path, mounted on a piezoelectric (PZT) ceramic. A different error signal is used to lock the squeezed beam to the LO. It is derived by the demodulation at the frequency Ω of the Radio Frequency (RF) difference signal provided by the

homodyne detector and sent to a PZT-mounted mirror in the LO path. Since the squeezed beam is phase-locked with this auxiliary beam, the implementation of this technique ensures the phase-locking of the squeezed beam with pump and LO beams. This allows us to have a stable squeezing angle, a fundamental requirement in order to have squeezing at the frequencies of interest for GW detection.

E. Optical phase-locked loop

In order to implement the techniques described in Sec. II D, two OPLLs are used to phase-lock the two laser sources Aux 1 and Aux 2 to the main laser, considered as the frequency reference (Fig. 1). A pick-off of this laser is overlapped after a Beam Splitter (BS) to a pick-off of each auxiliary lasers (with the same polarization and transverse field distribution as the main laser); the beat note generated at a photo-detector for each case acts as a Voltage-Controlled Oscillator (VCO) for the Phase-Locked Loop (PLL) electronic board, described in Sec. III A. The feedback control systems, which drive the tunable auxiliary lasers, enable having the required frequency shifts between these lasers and the free running main laser.

F. Homodyne detector

We use the balanced homodyne detection scheme[15] to measure the squeezing produced by our setup. In this scheme, the squeezed beam is superposed to a LO, i.e., a strong coherent field that we use as a phase reference. The balancing of optical and electronic components is crucial to obtain an accurate measurement of the squeezing factor. For this reason, we chose to use a 50/50 optical BS and to adopt a self-subtraction scheme in the detector electronic design: the difference of the photo-currents is obtained by taking the signal before any amplification from the node between the Photo-diodes (PDs) (D1 and D2). These are a high quantum efficiency (QE) (η ~99%) PDs, with a photosensitive area of 500× 500 μm^2, that operate in photo-conductive mode with a stabilized reverse bias. The homodyne detector provides the Direct Current (DC) readout of each PD, used for diagnostic and alignment, and an Alternating Current (AC) readout in the audio band [Audio Frequency (AF), 10 Hz–10 kHz] of the difference and sum of the photo-currents and in the radio band (RF, 1–100 MHz) of the difference photo-current (see Fig. 2). These readouts are obtained through a double stage amplification with two *trans*-impedance blocks that act as low-pass and high-pass filters in the relative band. The electronic components were chosen in order to keep the circuit dark noise of the differential readout at a level of 413 nV/$\sqrt{\text{Hz}}$ in the audio band and 220 nV/$\sqrt{\text{Hz}}$ in the radio band. The total power of the LO is 4 mW, which rises shot noise at the level of 6.52 μV/$\sqrt{\text{Hz}}$ in the audio channel, which gives 24 dB of clearance. In the radio channel, LO rises 596 nV/$\sqrt{\text{Hz}}$ of shot noise, which corresponds to 8.5 dB of clearance.

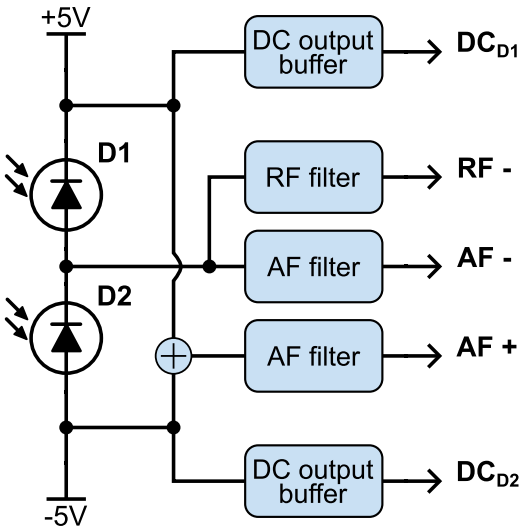

FIG. 2. Block diagram of the homodyne circuit design. The two photo-diodes are in the self-subtracting configuration[16] with the reverse bias of 5 V. Average light power impinging the PDs is detected through the DC output buffers. The difference of photo-currents is detected in the two different frequency bands: in AF (10 Hz–10 kHz, via AF filter) and in RF (1–100 MHz, via RF filter). The two photo-currents are also detected and summed in the AF band.

III. DIGITAL CONTROLS

As described in Secs. II A–II F, in order to produce squeezed vacuum states, many parameters of the setup have to be controlled: the length of the MZ interferometer, the temperature of the non-linear crystals, the frequency shifts between each auxiliary laser and the main laser, the phase of the pump and LO beams, and, finally, the length of the optical cavities. An important requirement for the control system is to be easily accessible to different scientists who work alternatively at the bench and with different expertise. Thus, its handling minimizes complex operation on the feedback controls, such as tuning or calibration. This is a first step toward a fully automated control system that minimizes human intervention and dead time, as required by a running GW detector. High level of automation helps us in the maximization of the subsystem QoS. Last but not least, we manage to keep the system compatible with the Virgo software and hardware infrastructure. We describe below the system developed by means of custom built devices as well as several devices manufactured for Virgo.

The whole experimental apparatus is controlled by an electronic system purposely designed for this application. Its schematic is shown in Fig. 3. Control loops used in the experiment can be divided in the following groups: PDH technique loops for longitudinal cavity lock, proportional-integral-derivative (PID) loops for MZ fringe lock and Coherent Control (CC), OPLLs, and temperature control loops. Direct Digital Synthesis (DDS) generators provide necessary modulation and demodulation signals. A detailed list of control loops is mentioned in Sec. II. All devices are remotely configurable and most of them are connected to Tango-based servers,[17] which extends the functionality of remote control to multi-user scenario. PDH technique loops and PID regulators are implemented as digital filters in Digital Signal Processing (DSP) units. After the introduction of this section, we describe the hardware for digital controls and then the software for its handling.

A. Hardware

All DDS generators share a common reference source in order to allow fixed phase between output signals. The reference source

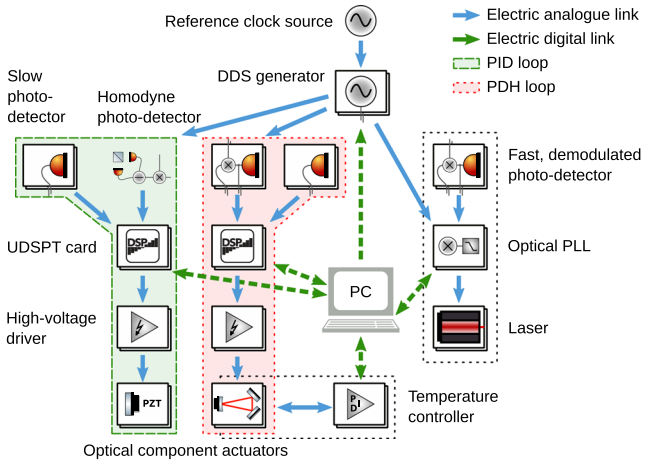

FIG. 3. Hierarchy and information flow chart in the electronic management system of the optical bench. Blue arrows show electric analog connections between single devices, while green arrows indicate digital communication links. Devices circled with the dashed-line form a PID loop, while devices circled with the dotted-line form a PDH technique loop. The pile symbol indicates that there are several devices of this kind in the system.

is based on the ADF4360 evaluation board that generates 500 MHz clock. The board is configured and monitored by a ATmega328 micro-controller for the correct operation. In case of failure, the generating chip is unconditionally reset. The micro-controller itself uses hardware watchdog to provide a high duty-cycle of the reference source. Watchdog timers are widely used in computer-controlled equipment where the hardware must rapidly react to faults.

There are two DDS units in the system. Each unit generates four independent sinusoidal signals. The first version of the DDS hardware is based on the AD9959 evaluation board for RF generation, and it requires a Personal Computer (PC) to be configured. The improved version is based on four AD9910 chips, and it has an embedded single-board computer (Aria G25) that integrates an ARM9 central processing unit (400 MHz), 256 MB of DDR2 RAM, and 10/100 Ethernet interface and hosts lightweight Linux distribution. The second version of the hardware provides much better Digital-to-Analog Converter (DAC) resolution and in consequence lower phase noise. Moreover, it gives the possibility of a remote control without a PC. This feature is an important facilitation for operators, however, digital links to the DDS and the PLL do not play active role in the automated locking. For this reason, it is not widely described.

In the experiment, we use two kinds of photo-detectors. A large-area, low bandwidth pre-amplified PD is used for light intensity monitoring, while a small-area, high bandwidth PD is used for cavity locking with the PDH technique and for the OPLL. A fast photo-detector circuit implements on-board analog demodulation if an external demodulation signal is provided.

OPLL uses a custom-made circuit based on an integrated PLL chip accompanied by a micro-controller. The circuit is designed to drive both laser frequency tuning inputs: internal piezo-actuator and laser crystal temperature. Despite the common error signal source for the two loops, we treat them independently. The division in the frequency band is due to the presence, in each laser, of the two distinct actuators with complementary transfer functions. Therefore, the PLL board includes two loop filters, an analog one for fast loop and a digital PID implemented in a micro-controller used also for monitoring the integrated error signal and for communication with the PC.

For temperature stabilization of the nonlinear crystals, we use a digital PID controller that reads two thermometers and drives a Thermoelectric Cooler (TEC). The controller is interfaced with the PC for parameter setting and temperature readout.

The core component of the system is the cards developed for Advanced Virgo Superattenuator control (UDSPT). UDSPT modules were developed for signal processing and real time control for the Virgo seismic isolation system (superattenuator)[18] and were upgraded for better performance.[19–21] Each module has six 24 bit Analog-to-Digital Converters (ADCs) and six 24 bit DACs sampled at a maximum frequency of 320 kHz. The software developed in a dedicated Software Development Kit (SDK) is executed within the chosen sampling time. The integrated DSP unit enables a numerically efficient implementation of high-order digital filters. UDSPTs provide advanced connectivity with the Virgo timing and Data AcQuisition (DAQ) system.[22] The newest version of the SDK enables the implementation FSM engine. We use this feature for quick lock acquisition of optical cavities. The algorithm we developed is described in Sec. III B.

Environmental monitoring is a standalone system compatible with Virgo monitoring software.[23–25] We access the real-time and the historical data about ambient temperature, atmospheric pressure, and air humidity via the PC managing our experiment. There are three thermometers in the laboratory covering the inside of the acoustic enclosure, clean air input flow, and electronic racks area. We use the data to verify the temperature stability, which has a direct impact on the misalignment of the optical setup (Fig. 10).

B. Software

The management system software architecture is shown in Fig. 4. The existing software is divided in three modules: a common

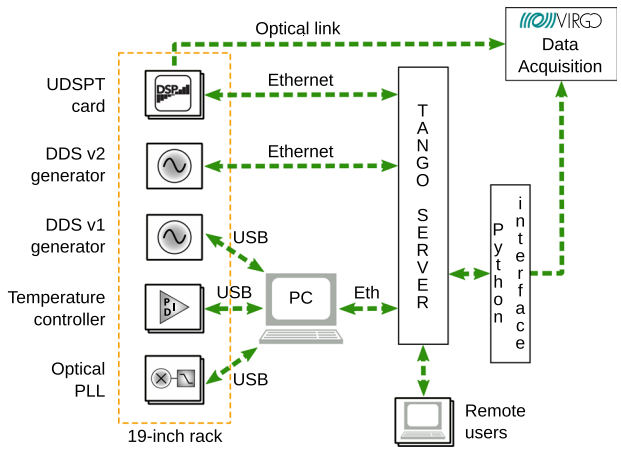

FIG. 4. Communication link architecture for the software development for the electronic management system of the optical setup. Green arrows indicate digital communication links. Components placed inside the pile symbol are numerous.

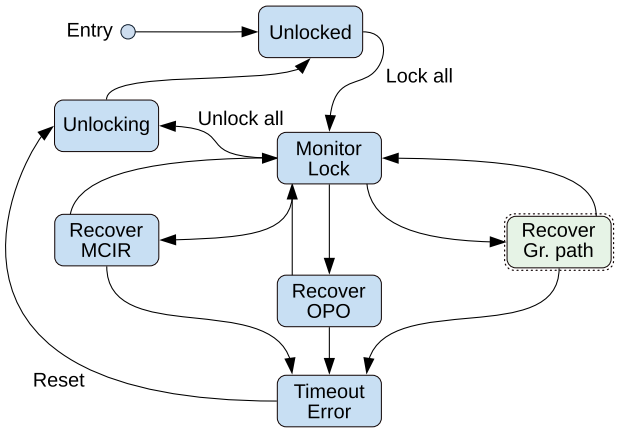

FIG. 5. Finite state machine for lock acquisition, monitor, and recovery of the whole bench. When the machine is launched, it enters the *Unlocked* state. It switches states automatically except the three manually triggered transitions: *Lock all*, *Unlock all,* and *Reset*. The machine leaves *Monitor lock* automatically when any of the monitored devices need to be recovered. *Gr. path* stands for the green light path, and its operation is managed by another FSM. Recovery of monitored components can be executed in parallel.

Graphical User Interface (GUI) that implements also the slow part of the management logic; a UDSPT software implementing feedback loops and FSMs for fast lock logic; and a firmware dedicated for each independent device such as reference clock source, OPLL, and DDS.

Slow logic is a part of the GUI script written in Python. The logic is implemented as a FSM, and it constitutes the back end of GUI. It drives all locking loops managed by the UDSPTs: MCIR, OPO, SHG, MCG, MZ, pump beam coherent control (CC_{PUMP}), and local oscillator coherent control (CC_{LO}). The structure of the slow FSM is split into two and shown in Figs. 5 and 6. The latter is nested in the former one and it takes care of the lock of the three devices in series conditioning green light, which are SHG, MCG, and MZ. Communication to the fast FSM is provided via two unidirectional variables: *Requested state* and *Actual state*. The slow logic algorithm is executed in one second interval. In each iteration, it checks transition conditions and acts adequately. One of the monitored conditions is the value of the variable *Requested state*. The variable can have three values: *Lock all*, *Unlock all,* and *Reset*. After the complete cycle, the machine updates *Actual status* to indicate its current state. CC loop can be engaged by the monitor lock only if the squeezing is produced.

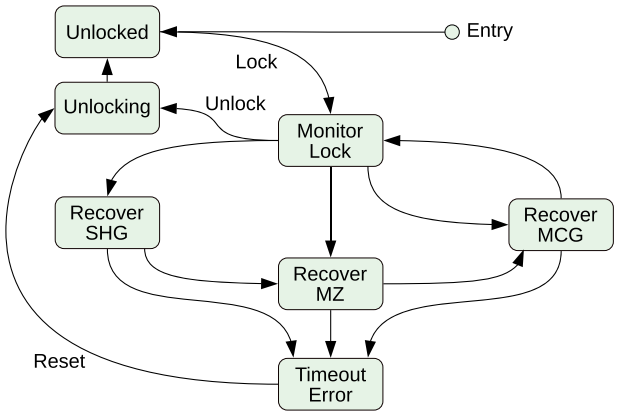

FIG. 6. Finite state machine for lock acquisition, monitor, and recovery of the green light path. When the machine is launched, it immediately enters the *Monitor lock* state. Then, it leaves the *Monitor lock* state to recover the monitored devices and goes back to the monitoring. In this machine, the lock sequence is maintained in order to assure a correct lock of subsequent devices.

Each optical cavity, MZ, and CC loop are managed by a dedicated FSM implemented in the UDSPT. The structure of this FSM is described in Ref. 26. In our case, ADCs sample at 160 kHz. FSM has two stable states: UNLOCKED and LOCKED. It performs calibration at the beginning of each lock procedure and manages automatic relocking during operation. The calibration step is important from the automation point of view. During the calibration, the algorithm acquires outermost values of transmission signals and the mean value of error signal. All FSMs are managed by the code underlying GUI, which implements simple logic for high level automation.

For visualization of digitized signals in the experiment, we use dataDisplay software.[27] This tool was developed for the Virgo experiment. It is used to process and visualize the online data with low latency to help the commissioning and the analysis of the Virgo interferometer.

We implemented and tested algorithms presented in this section. The analysis is described in Sec. IV D.

IV. EXPERIMENTAL RESULTS

In this section, the experimental results are described. In particular, in Secs. IV A and IV B, the lock sequence for the control of the optical cavities and the PID controls are shown, respectively. In Sec. IV C, a preliminary squeezing measurement is presented. Finally, in Sec. IV D, the quality of service is discussed.

A. Control of optical cavities

The two nonlinear cavities (SHG and OPO) and the two triangular mode cleaner cavities (MCIR and MCG in Fig. 1) are locked using the PDH technique.[14] SHG and MCIR must be resonant at the same frequency of the squeezed field; hence, the locking beam is provided by the main laser modulated at 80 MHz. The OPO locking beam comes from the Nd:YAG laser (Aux 2) modulated at the same frequency, while the MCG is locked using the second harmonic beam, provided by the SHG cavity and modulated at 30 MHz. Table II shows the fundamental mode content for transmitted power of each cavity. In Fig. 7, a longitudinal lock sequence for an optical cavity, in particular, for the MCG, has been shown. In the first panel, we show the piezoelectric actuator driving signal, in the second one, the error signal, and in the third one, the cavity transmission. The cavity, initially, is in an *Unlocked* state. The lock acquisition sequence starts after a manual command given through

TABLE II. Fundamental mode content for the transmitted power of each cavity.

SHG	MCG	OPO	MCIR
91%	90%	93%	93%

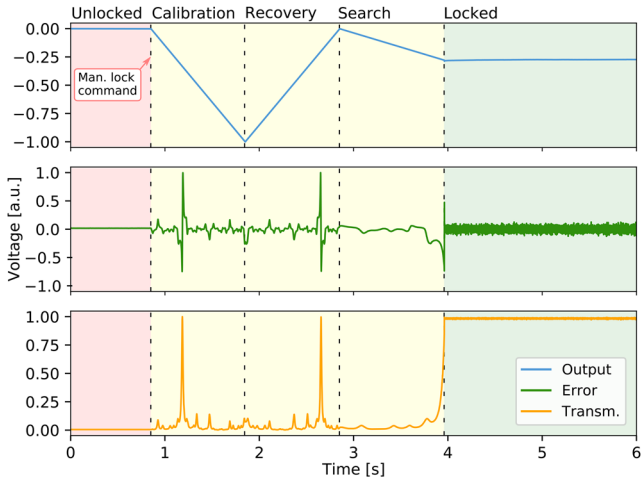

FIG. 7. PDH technique loop lock after manual command includes the calibration step. Each panel represents the electric signal: controller output, error signal, and optical power on the photo-detector in the transmission of the cavity. Background color indicates lock phases: red—unlocked, yellow—locking, and green—locked. The locking phase is divided into calibration, recovery, and search step, which is indicated above. The moment when the manual lock command is issued is indicated by the tag.

the GUI. The first phase of this sequence is *calibration*, followed by a *recovery*. During the former phase, the algorithm tests the input signal range and in the latter, it goes back to the center of the actuator dynamic range in order to avoid a frequent piezo-return at the saturation. After these two steps, it enters in the *Search* phase where the system tries to find the transmission peak. Once found, the cavity length is controlled and the system enters in a *Locked* status.

B. Control of Mach–Zehnder interferometer and coherent control

MZ length control, CC_{PUMP}, and CC_{LO} loops are implemented using PID controllers. Figure 8 shows the lock sequence in the case of the MZ interferometer (see Sec. II B), after the manual lock command, given when the system is in an *Unlocked* state. The piezoelectric driving signal and the transmission fringes are shown in the first and second panel, respectively. After the calibration, the system passes immediately to locked state. In the specific case, this means that the MZ interferometer output signal is constant in time and the OPO pump beam power is stable. The same logic is used for the CC technique, described in Sec. II D. Here, two loops have been implemented, one to fix the phase between the CCB and the pump beam (CC_{PUMP}) and the other to fix the phase between the same CCB and the LO beam.

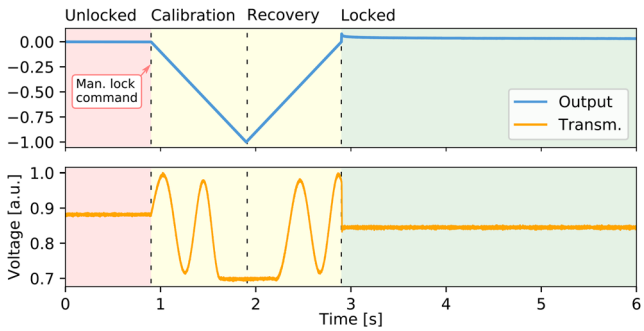

FIG. 8. PID loop lock sequence after manual command includes the calibration step. The upper panel represents the controller output electric signal, while the lower panel shows the error signal that in the PID loop case is the optical power on the photo-detector in the transmission of MZ.

C. Squeezing level and optical losses

Figure 9 showcases the measurement of SN reduction using squeezed vacuum, performed at 1 MHz of detection frequency. In this figure, dark noise, LO shot noise, and the measured squeezing and anti-squeezing are plotted in orange, green, and blue, respectively. The purple line represents the estimated level of squeezing that the OPO cavity can produce, calculated from the measured level of squeezing and taking into account the squeezing degradation due to optical losses. The measured squeezing level is −5.7 dB, and the anti-squeezing level is 14.7 dB. The squeezing measurement has been performed changing the relative phase between the beam produced by the OPO and the LO by scanning the pump beam phase with a triangular ramp signal at 120 Hz. The pump power for the OPO in our measurement is 69 mW, and the LO power is 4 mW. The measurement is performed in the time domain by setting the spectrum analyzer in the zero-span mode with a central frequency of 1 MHz at 300 kHz of Resolution Bandwidth (RBW) and a time window of 20 ms is set.

Starting from the squeezing and anti-squeezing variance measurement, it is easy to find the OPO achievable squeezing variance (or produced squeezing and anti-squeezing level) by using the following relationship:

$$V_{\pm}^{\text{meas}} = \eta_{\text{tot}} V_{\pm}^{\text{prod}} + (1 - \eta_{\text{tot}}), \tag{1}$$

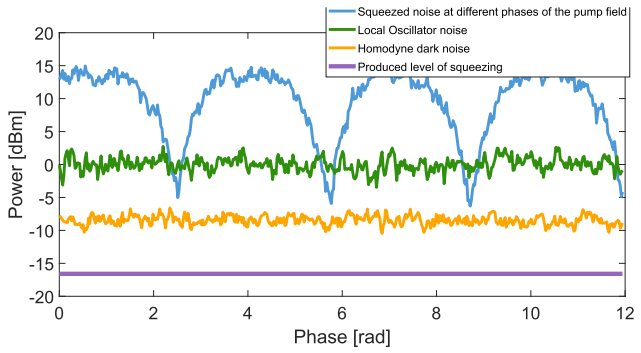

FIG. 9. Preliminary squeezing measurement in the radio frequency band. The characterization is performed at 1 MHz of Fourier frequency with 300 kHz of RBW, and a time window of 20 ms is set on the spectrum analyzer. The three plotted curves represents the homodyne dark noise (orange curve), the LO shot noise (green curve), the injected squeezing at different phases of the pump field (blue curve), and our OPO produced squeezing (purple curve).

TABLE III. Optical efficiency budget for the calculation of produced squeezing.

	η_{prop}	η_{esc}	v^2	η_q	η_{tot}
Budget (%)	84.7	94.9	94	99	74.8

where V_+ and V_- are, respectively, the anti-squeezing and squeezing variances, with V_{prod} being the achievable variance and V_{meas} being the measured variance. η_{tot} is the total optical efficiency that includes all the losses from the generation to the detection of squeezed light. The calculation of the optical losses L includes the propagation efficiency η_{prop}, the PD quantum efficiency η_q, the OPO escape efficiency η_{esc}, and the homodyne mismatch measured with the fringe visibility v. Thus, the overall optical losses can be computed, given the total efficiency η_{total},

$$\eta_{total} = v^2 \eta_q \eta_{esc} \eta_{prop}. \quad (2)$$

Each efficiency and the total efficiency are shown in Table III. In the following, we will describe the computation of each contribution to the total optical efficiency.

The propagation losses include those of the infrared light transmission of the harmonic BS (equal to 0.5%), those of the PBS (equal to 0.5%), and the ones from other optics including lenses, mirrors, and half-wave plate (experimentally equal to 3.8%). Moreover, the beam diameter for the two beams arriving in the two photo-diodes of the homodyne detector has been over-sized compared to the adapted beam waist for the homodyne detector (31 μm), and the waist position of each beam falls at the middle distance between the two photodetectors. Hence, a fraction of the beam power is clipped by the two detectors, and by estimating this loss with a Gaussian probability distribution function, the results obtained is 94.3% for the fraction of power collected by each detector. The total propagation losses are equal to 15.3%.

The escape efficiency of a squeezed light source is defined as

$$\eta_{esc} = \frac{T}{T+L}, \quad (3)$$

where $T = 0.08$ is the transmission of the output coupling mirror and L the is intracavity Round-Trip Losses (RTLs). These include the PPKTP losses due to the residual transmission through the HR-coated backside (0.025%); the (negligible) absorption within the crystal is 12 ppm/cm, and the residual reflection of the AR-coated frontside (0.2%)must be taken into account two times. Thus, RTL ~0.43%; hence, $\eta_{esc} = 0.949$.

According to Eq. (1), with $\eta_{tot} = 0.748$, the produced squeezing level of our OPO is −16.4 dB; this value does not take into account the dark noise of the homodyne detector and the effect of phase-noise.

D. Service quality

The digital control system described in this paper is characterized by two parameters: lock acquisition time of an uncalibrated loop, measured separately for each loop, and statistics of uptime during a test period also calculated for each loop. The uptime statistics were registered in almost eight consecutive days (189.5 h) by a dedicated monitoring script. The running script registered each transition of all fast FSMs. The data acquired during the test period are plotted in Fig. 10. The temperature of the experiment was stable during the first half of the test. In the second half, we observe distinct fluctuations corresponding to day and night changes. As the laboratory is placed in a non-thermalized building, the fluctuations are certainly related to the increased daily change of the environment temperature caused by unfavorable weather conditions. The status of each loop is plotted in the second panel as a binary value where high state corresponds to *Locked* state. We measured the lock acquisition time, including calibration step, using another technique by means of the internal timer of the UDSPT. In this measurement, the status of an uncalibrated loop has any loop in the system that needs to pass the calibration state in the FSM before the lock acquisition. The statistics of uptime were measured by a script monitoring status of all loops in an engaged state and registering transition date and time. Acquired data were post-processed, and the results are shown in Table IV.

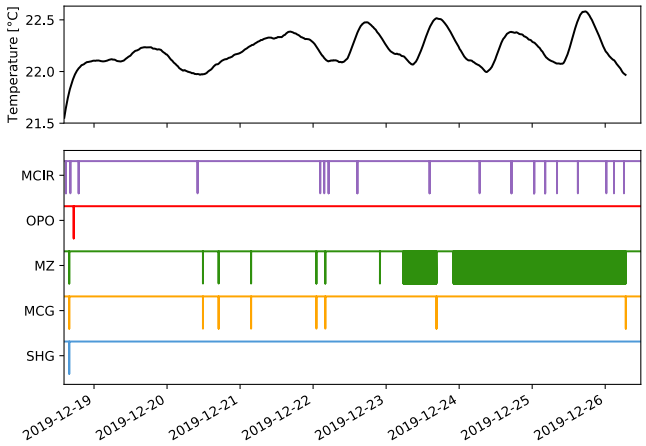

FIG. 10. Visualization of data characterizing QoS in time. The upper panel shows the temperature trend of the optical setup. In the lower panel, each row indicates binary state of monitored loop.

The recovery time of the entire green light path was measured separately and it takes 12 s. The low QoS of the MZ, with respect to

TABLE IV. Characterization of quality of locking. In the first column, the time necessary to acquire lock of the longitudinal degree of freedom with corresponding uncertainty is given. The column titled QoS shows the amount of time in which the loop remained lock with respect to the total time of the measurement. In the last column, we report the total time the loop was out of service during the testing period. The MZ loop is the only PID loop characterized in the set. Its locking sequence comprises only the arbitrary calibration and recovery time; thus, its variance is not reported.

	Lock acquisition mean time (s)	QoS (%)	Out of service total time (s)
SHG	2.7(1)	99.9995	2
MCG	2.4(2)	99.9964	23
MZ	2.0	81.53	238 477
OPO	3.1(2)	99.9995	2
MCIR	4.0(4)	99.9726	185

the other loops, can be explained by a small dynamic range of actuation due to a slightly too low visibility of the MZ interferometer during QoS data acquisition period. An increase in the MZ visibility would give enough actuation range and then a subsequent improvement of the MZ QoS, while the choice of a not too high visibility value will still keep the MCG immune from MZ unlocks. By preserving this careful MZ visibility trade-off, we should reach a QoS of 99.9%. The locking time of loops meets the requirements for a reliable GW detector subsystem given in Ref. 8. Considering the very feasible improvement of the MZ, the duty cycle may easily exceed 99.9%.

V. CONCLUSIONS

The system described in this paper is a complete, robust, and stable optical setup for squeezed light generation with high degree of automation, suitable for experiments on advanced quantum optics methods for gravitational-wave detectors. The stability of the system has been proven in the direct measurement of QoS. Quantum noise is a major limitation to the sensitivity of GW detectors. Reducing the downtime of a squeezed light source may have an impact on the detection rate of a GW observatory, which depends on both the noise background and the experimental duty-cycle. The described facility, including developed software, can be easily scaled for experiments on alternative use of squeezing states in gravitational-wave detectors[28] or as a reference source for research on ponderomotive squeezing.[29]

AUTHORS' CONTRIBUTIONS

M.B. realized the software based on finite state machines. He also dealt with the electronics and control system. V.S. and C.N. contributed to the realization of the optical setup and optical measurements. They also tested the performances of the finite state machine based software. L.N., A.G., F.P., D.P., M.P., L.C., M.V., and J.-P.Z. provided a part of the electronic equipment and contributed to the software and control system. I.K., M.L., L.G., S.D.P., M.B., G.C., L.C., B.D., B.G., M.D.L., and F.S. contributed to the optics. The contribution of I.K., M.L., and M.V. and part of the contribution of V.S. are proved by their Ph.D. theses.[30–33] The contributions of L.G. and B.G. are proved by their master theses.[34,35] M.D.L. and F.S. coordinated this work. R.D.R. and L.D.F. provided the environmental monitoring. M.B., C.N., M.B., V.S., S.D.P., L.N., and I.K. wrote the draft. J.-P.Z., E.C., V.F., E.M., F.R., A.R., and H.V. took care about the organization and the procurement of funding and instrumentation.

ACKNOWLEDGMENTS

The authors gratefully acknowledge the Italian Istituto Nazionale di Fisica Nucleare (INFN) for financial support and the French Centre National de la Recherche Scientifique (CNRS) for the creation and support of the EGO consortium together with INFN.

F.S. and V.S. acknowledge the Italian Ministry of Education, University and Research (MIUR) for financial support under the PRIN project (No. 2015L33WAK_002).

C.N. acknowledges the EGO consortium for financial support during this work.

During this work, M.B. was supported by the COST Action CA17137.

DATA AVAILABILITY

The data that support the findings of this study are available from the corresponding authors upon reasonable request.

REFERENCES

[1] B. P. Abbott, R. Abbott, T. Abbott, M. Abernathy, F. Acernese, K. Ackley, C. Adams, T. Adams, P. Addesso, R. Adhikari *et al.*, "Observation of gravitational waves from a binary black hole merger," Phys. Rev. Lett. **116**, 061102 (2016).

[2] B. Abbott, R. Abbott, T. Abbott, S. Abraham, F. Acernese, K. Ackley, C. Adams, R. Adhikari, V. Adya, C. Affeldt *et al.*, "GWTC-1: A gravitational-wave transient catalog of compact binary mergers observed by LIGO and Virgo during the first and second observing runs," Phys. Rev. X **9**, 031040 (2019).

[3] B. Abbott, R. Abbott, T. Abbott, S. Abraham, F. Acernese, K. Ackley, C. Adams, R. Adhikari, V. Adya, C. Affeldt *et al.*, "GWTC-2: Compact binary coalescences observed by LIGO and Virgo during the first half of the third observing run," 2020; accessed 12 January 2021.

[4] C. M. Caves, "Quantum-mechanical noise in an interferometer," Phys. Rev. D **23**, 1693 (1981).

[5] R. Slusher, L. Hollberg, B. Yurke, J. Mertz, and J. Valley, "Observation of squeezed states generated by four-wave mixing in an optical cavity," Phys. Rev. Lett. **55**, 2409 (1985).

[6] H. Vahlbruch, S. Chelkowski, B. Hage, A. Franzen, K. Danzmann, and R. Schnabel, "Coherent control of vacuum squeezing in the gravitational-wave detection band," Phys. Rev. Lett. **97**, 011101 (2006).

[7] J. Abadie, B. P. Abbott *et al.*, "A gravitational wave observatory operating beyond the quantum shot-noise limit," Nat. Phys. **7**, 962–965 (2011).

[8] F. Acernese, M. Agathos, L. Aiello, A. Allocca, A. Amato, S. Ansoldi, S. Antier, M. Arène, N. Arnaud, S. Ascenzi *et al.*, "Increasing the astrophysical reach of the advanced virgo detector via the application of squeezed vacuum states of light," Phys. Rev. Lett. **123**, 231108 (2019).

[9] M. Tse, H. Yu, N. Kijbunchoo, A. Fernandez-Galiana, P. Dupej, L. Barsotti, C. Blair, D. Brown, S. Dwyer, A. Effler *et al.*, "Quantum-enhanced advanced LIGO detectors in the era of gravitational-wave astronomy," Phys. Rev. Lett. **123**, 231107 (2019).

[10] M. Bawaj, M. D. Laurentis, S. D. Pace, A. Gennai, I. Khan, E. Majorana, L. Naticchioni, C. Nguyen, D. Passuello, V. Sequino, F. Sorrentino, M. Vardaro, and J.-P. Zendri (2020). "Electronic hardware and software development for EPR squeezer," Zenodo. https://doi.org/10.5281/zenodo.3554362.

[11] H. Vahlbruch, M. Mehmet, K. Danzmann, and R. Schnabel, "Detection of 15 dB squeezed states of light and their application for the absolute calibration of photoelectric quantum efficiency," Phys. Rev. Lett. **117**, 110801 (2016).

[12] M. Leonardi, M. Bazzan, L. Conti, M. Pegoraro, G. A. Prodi, M. Vardaro, and J.-P. Zendri, "Efficient second harmonic generation with compact design: Double-pass and cavity configurations," Laser Phys. **28**, 115401 (2018).

[13] A. Khalaidovski, H. Vahlbruch, N. Lastzka, C. Gräf, K. Danzmann, H. Grote, and R. Schnabel, "Long-term stable squeezed vacuum state of light for gravitational wave detectors," Classical Quantum Gravity **29**, 075001 (2012).

[14] E. D. Black, "An introduction to Pound–Drever–Hall laser frequency stabilization," Am. J. Phys. **69**, 79–87 (2001).

[15] M. Stefszky, C. Mow-Lowry, S. Chua, D. Shaddock, B. Buchler, H. Vahlbruch, A. Khalaidovski, R. Schnabel, P. K. Lam, and D. McClelland, "Balanced homodyne detection of optical quantum states at audio-band frequencies and below," Classical Quantum Gravity **29**, 145015 (2012).

[16] K. McKenzie, N. Grosse, W. P. Bowen, S. E. Whitcomb, M. B. Gray, D. E. McClelland, and P. K. Lam, "Squeezing in the audio gravitational-wave detection band," Phys. Rev. Lett. **93**, 161105 (2004).

[17] See https://tango-controls.readthedocs.io/en/latest/ for Tango Community, Tango controls documentation, 2019; accessed 3 October 2019.

[18]F. Acernese *et al.*, "The real-time distributed control of the virgo interferometric detector of gravitational waves," IEEE Trans. Nucl. Sci. **55**, 302–310 (2008).
[19]A. Gennai, D. Passuello, V. Boschi, G. Cerretani, C. Magazzu, M. Bitossi, C. Carissimi, and L. Rei, VIR-0374A-15 A new high performance suspension control system for advanced Virgo, https://tds.virgo-gw.eu/, 2015; accessed 21 December 2019.
[20]A. Gennai, VIR-0541A-16 UDSPT board output noise, https://tds.virgo-gw.eu/, 2016; accessed 21 December 2019.
[21]M. Bitossi, A. Gennai, and D. Passuello, "A/D and D/A processing unit for real time control of suspended masses in advanced virgo interferometer," https://tds.virgo-gw.eu/ql/?c=14806, 2019; accessed 21 December 2019.
[22]F. Acernese *et al.*, "Data acquisition system of the virgo gravitational waves interferometric detector," IEEE Trans. Nucl. Sci. **55**, 225–232 (2008).
[23]R. De Rosa, VIR-0534A-14 plans for environmental monitoring electronics, https://tds.virgo-gw.eu/, 2014.
[24]I. Fiori, R. De Rosa, and F. Paoletti, VIR-0269A-19 A short newcomers's guide to AdV Environmental Monitoring, https://tds.virgo-gw.eu/, 2019.
[25]F. Barone, R. De Rosa, A. Eleuteri, L. Milano, and K. Qipiani, "The environmental monitoring system of VIRGO antenna for gravitational wave detection," IEEE Trans. Nucl. Sci. **49**, 405–410 (2002).
[26]M. Bawaj, V. Sequino, C. Nguyen, M. Vardaro, S. D. Pace, I. Khan, D. Passuello, A. Gennai, M. D. Laurentis, J.-P. Zendri, and F. Sorrentino, "Finite state machine controls for a source of optical squeezed vacuum," arXiv:2004.00316 [physics.ins-det] (2020).
[27]LAPP Virgo group, Virgo data Display documentation, http://lappweb.in2p3.fr/virgo/dataDisplay/, 2019; accessed 3 January 2020.
[28]Y. Ma, H. Miao, B. H. Pang, M. Evans, C. Zhao, J. Harms, R. Schnabel, and Y. Chen, "Proposal for gravitational-wave detection beyond the standard quantum limit through EPR entanglement," Nat. Phys. **13**, 776–780 (2017).
[29]S. D. Pace, L. Naticchioni, E. Majorana, L. Giacoppo, P. Puppo, F. Ricci, P. Rapagnani, M. Perciballi, M. D. Laurentis, E. Calloni, F. Travasso, M. Bawaj, H. Vocca, A. Piluso, V. Sequino, and F. Sorrentino (2020). "Small scale suspended interferometer for ponderomotive squeezing (SIPS) as test bench for EPR squeezer integration in advanced Virgo," Zenodo. https://doi.org/10.5281/zenodo.3569196.
[30]I. Khan, "Squeezed states of light generation for short noise limited interferometric measurements in the next generation of gravitational waves detectors," Ph.D. thesis, Gran Sasso Science Institute, 2019.
[31]M. Leonardi, "Development of a squeezed light source prototype for advanced Virgo," Ph.D. thesis, University of Trento, 2016.
[32]M. Vardaro, "Toward a fully automated and digitally controlled squeezed vacuum source," Ph.D. thesis, Università degli Studi di Padova, 2018.
[33]V. Sequino, "Development of a squeezed light source for the gravitational wave detector advanced Virgo," Ph.D. thesis, Università degli Studi di Roma "Tor Vergata", 2016.
[34]L. Giacoppo, "Squeezed vacuum generation for quantum noise reduction in GW detectors," M.Sc. thesis, Università degli Studi di Roma "Tor Vegata", 2017.
[35]B. Garaventa, "Towards an Einstein–Podolsky–Rosen experiment for quantum noise reduction in gravitational wave detectors," M.Sc. thesis, Università degli Studi di Genova, 2018.